Biosensors and Bioelectronics 290 (2025) 117964

Contents lists available at ScienceDirect

Biosensors and Bioelectronics

journal homepage: www.elsevier.com/locate/bios

Ultrasensitive multifunctional biosensor integrating ECL quenching and DPV enhancement for early classification of thyroid cancer via BRAF V600E and microRNA-221 detection

Yan Zhang [a], Zhuoxin Ye [a], Mo Ma [a,b], Yongli Wu [a], Yuxuan Chen [a], Ruiyan Liu [a], Pinyi Ma [a,*], Daqian Song [a,**]

[a] *College of Chemistry, Jilin Province Research Center for Engineering and Technology of Spectral Analytical Instruments, Jilin University, Qianjin Street 2699, Changchun, 130012, China*

[b] *School of Pharmacy, Jilin University, Qianjin Street 2699, Changchun, 130012, China*

ARTICLE INFO

Keywords:
Electrochemiluminescence
CdTe-DNA quantum dots
BRAF V600E mutation
MicroRNA-221
Thyroid cancer diagnosis

ABSTRACT

Papillary thyroid carcinoma (PTC) is the most prevalent form of thyroid cancer with a high incidence among endocrine malignancies. It tends to metastasize early in lymph nodes and differs markedly from other subtypes in biological behavior, clinical management, and prognosis. Therefore, accurately distinguishing PTC from other pathological subtypes is crucial for guiding diagnosis and treatment decisions. However, conventional methods such as thyroid ultrasound and ultrasound-guided fine-needle aspiration cytology (FNA) have limitations, including sampling errors and low sensitivity. To address these challenges, we developed a novel electrochemiluminescence (ECL) biosensor from CdTe-DNA quantum dots (QDs) and an enzyme-free DNA amplification circuit. In the system, toehold-mediated strand displacement reactions (TSDR) were utilized to generate Cy5-modified DNA strands, which quench the ECL signal via an energy transfer effect. The quenching indicates the presence of thyroid cancer. Catalytic hairpin assembly (CHA) was employed to produce ferrocene (Fc)-labeled DNA strands to enable dual-mode signal modulation (ECL quenching and differential pulse voltammetry (DPV) enhancement) for accurate classification of PTC. Validation experiments demonstrated that the biosensor exhibits excellent sensitivity and a broad dynamic range, enabling the simultaneous detection of BRAF V600E mutations and microRNA-221 (miR-221) expression. This integrated sensing platform offers is a promising tool for the early diagnosis and molecular classification of thyroid cancer.

1. Introduction

Thyroid cancer ranks as the seventh most commonly diagnosed malignancy worldwide, according to the 2024 global cancer statistics (Bray et al., 2024). It comprises four major pathological types: papillary thyroid carcinoma (PTC), follicular thyroid carcinoma (FTC), medullary thyroid carcinoma (MTC), and anaplastic thyroid carcinoma (ATC) (Boucai et al., 2024; Tickoo et al., 2000; Xu et al., 2024; Zhang et al., 2024). These subtypes have different biological behavior, therapeutic response, and clinical outcomes. For instance, PTC tends to metastasize to lymph nodes during an early stage, whereas FTC and MTC are prone to hematogenous dissemination. Moreover, radioactive iodine (RAI) therapy is highly effective in PTC, but ineffective in MTC and ATC; it can potentially delay the initiation of more appropriate, targeted therapies (Bikas et al., 2016; Cabanillas et al., 2016; Davis et al., 2023; Giovanella et al., 2022; Haddad et al., 2018; Mishra et al., 2023). Therefore, the ability to distinguish between PTC and other subtypes is essential for optimizing treatment strategies and improving prognosis.

Thyroid ultrasound and ultrasound-guided fine-needle aspiration cytology (FNA) are the current standard tools for diagnosing thyroid nodules (Haugen et al., 2016). However, these approaches are limited by low sensitivity, insufficient resolution for preoperative staging, and sampling errors in cytological evaluation (Brauckhoff and Biermann, 2020; Cappola, 2017; Eilers et al., 2014; Maeda et al., 2025; Yeh et al., 2004). These gaps underscore the urgent need for more accurate molecular detection strategies to improve the clinical identification and

---

* Corresponding author.
** Corresponding author.
E-mail addresses: mapinyi@jlu.edu.cn (P. Ma), songdq@jlu.edu.cn (D. Song).

https://doi.org/10.1016/j.bios.2025.117964
Received 21 July 2025; Received in revised form 2 September 2025; Accepted 3 September 2025

stratification of PTC.

The BRAF gene encodes a serine/threonine kinase involved in the regulation of cell proliferation, differentiation, and apoptosis. The most prevalent oncogenic variant, BRAF V600E, is found in various tumors, particularly thyroid cancer, and serves as a key molecular marker for cancer diagnosis and prognosis (Giovanella et al., 2022; Kurt et al., 2012; McFadden et al., 2014; Tan et al., 2020; Veschi et al., 2023). Although next-generation sequencing (NGS) and allele-specific PCR are commonly used for BRAF V600E detection, each method has notable drawbacks. While NGS is time-consuming and technically demanding, allele-specific PCR lacks sensitivity required for detecting mutations with ultra-low abundance (Kouba et al., 2018; Pellegrini et al., 2018). These limitations highlight the need for rapid, ultrasensitive mutation detection platforms.

MicroRNAs (miRNAs) are non-coding single-stranded RNAs that play pivotal roles in regulating oncogenesis. Alterations in miRNA expression often precede the onset of clinical symptoms and traditional biomarkers; thus, they are promising candidates for early cancer diagnosis (Laukienė et al., 2022; Mahmoudian-Sani et al., 2017). Specifically, miR-221 is overexpressed in PTC and exhibits a synergistic effect with BRAF V600E mutations, which helps further enhance its diagnostic value (Liang et al., 2018; Park et al., 2021). However, the detection of miRNAs remains technically challenging due to their low abundance, short length, and sequence homology.

Electrochemiluminescence (ECL), a technique integrating electrochemical and luminescent detection, has high sensitivity, fast response, and excellent controllability, making it a powerful technique in analytical chemistry (Chen et al., 2024; Meng et al., 2023; Wang et al., 2019; Wei et al., 2023; Yang et al., 2024; Ye et al., 2023; Zhou et al., 2022). ECL has been employed in various biosensing applications, including clinical diagnostics, food safety, and environmental monitoring (Liu et al., 2020; Zhang et al., 2017; Zhou et al., 2020, 2022). It is particularly suited for nucleic acid analysis, including miRNA detection (Lei et al., 2024; Li et al., 2024).

In this study, we developed a multifunctional ECL biosensor based on enzyme-free DNA amplification and CdTe-DNA QDs for the simultaneous detection of BRAF and miR-221. We used toehold-mediated strand displacement reactions (TSDR) as the BRAF V600E mutation recognition moiety and catalytic hairpin assembly (CHA) as the miR-221 detection element. This dual-mode sensing platform combines ECL signal quenching with DPV enhancement, offering a sensitive, specific, enzyme-free approach for the diagnosis and classification of PTC.

2. Experimental section

2.1. Synthesis of CdTe-DNA QDs

A NaHTe solution was freshly prepared by mixing 25 mg of $NaBH_4$ with 40 mg of tellurium powder in 1 mL of deoxygenated deionized water at 70 °C for 1 h under nitrogen protection. The mixture was placed in a sealed centrifuge tube with a syringe needle on the cap to allow the release of hydrogen gas generated from the reaction. The $CdCl_2$-MPA precursor solution was prepared by mixing 2.00 mM $CdCl_2$ with 2.00 mM 3-mercaptopropionic acid (MPA) in deionized water. The pH was adjusted to 9.0 using 0.1 M NaOH, and the solution was stored at 4 °C. For QD synthesis, 500 μL of the precursor solution was mixed with 2.0 μL of freshly prepared NaHTe and then diluted with 500 μL of deionized water to a final volume of 1 mL. The reaction mixture was transferred to a thermal shock reactor where it was heated at 100 °C for 3 h. To terminate the reaction, the solution was immediately cooled to room temperature in an ice-water bath (Tikhomirov et al., 2011). The resulting CdTe-DNA QDs emitted red fluorescence at 615 nm. The product was purified using ultrafiltration centrifuge tubes (30 kDa molecular weight cutoff) to remove excess salts and free DNA. Specifically, 1 mL of the CdTe-DNA QDs solution was centrifuged at 8000 rpm for 5 min, and then concentrated to a final volume of 50 μL.

2.2. Assembly of TSDR and CHA circuits

All oligonucleotides (L, S, T, F, FL, LOCKER, SIGNAL, H1, and H2) were dissolved in TE buffer and diluted with Tris-HCl buffer to prepare working solutions.

For the TSDR reaction, the L–S–T ternary complex was formed by annealing equimolar concentrations (3 μM each) of strands L, S, and T. The mixture was heated to 95 °C for 10 min and gradually cooled to room temperature. Fuel strands, F–FL and LOCKER–SIGNAL (20 μM each), were prepared under the same conditions. The target BRAF sequence was incubated with the preassembled L–S–T complex and F–FL strands at 37 °C for 2.5 h. The reaction products containing the S strand were stored at 4 °C for further use.

For the CHA reaction, hairpin probes, H1 and H2 (2 μM each), were annealed and cooled to 25 °C. The H1/H2 mixture was then incubated with different concentrations of miR-221 at 37 °C for 2 h. The resulting products were stored at 4 °C. The assembly of both circuits was verified by PAGE.

2.3. Measurement

For BRAF V600E detection, 8 μL of the reaction product was applied to the surface of the functionalized electrode and incubated at 37 °C for 2 h to allow hybridization with the immobilized capture probes. The electrodes were then rinsed with deionized water to remove unbound species, and the ECL signal was recorded. Similarly, for miR-221 detection, 8 μL of the reaction solution was applied to the electrode and incubated at 37 °C for 2.5 h. After rinsing, ECL and DPV measurements were performed. ECL measurements were conducted using an MPI-E ECL analyzer in 3 mL of 0.1 M phosphate-buffered saline (PBS, pH 7.4) containing 10 μL of triethylamine (TEA). The potential was scanned from −0.5 to +1.2 V at a rate of 500 mV/s. DPV measurements were performed using a CHI 760E electrochemical workstation in 5 mL of 0.1 M PBS (pH 7.4). The potential range was from 0 to +0.8 V vs. Ag/AgCl, and the scan rate was 100 mV/s.

3. Results and discussion

3.1. Design principle of the biosensor

The working principle of the proposed biosensor in detecting BRAF V600E and miR-221 is illustrated in Scheme 1. CdTe-DNA QDs were first employed as ECL emitters to construct a "signal-on" baseline platform. For BRAF V600E detection, TSDR was implemented based on the principle of free energy minimization. In the presence of BRAF V600E, the TSDR process is triggered, thereby generating a large number of S-strands while enabling target recycling. These S-strands then bind competitively to the LOCKER probes, displacing the Cy5-labeled SIGNAL strands. The released SIGNAL strands are subsequently captured by complementary probes immobilized on the electrode surface. Due to energy transfer between CdTe QDs and Cy5, the ECL signal is quenched, leading to the switching of the system from a "signal-on" to a "signal-off" state, which is the indication of the presence of thyroid cancer.

For miR-221 detection, a CHA amplification circuit was employed, and two hairpin probes (H1 and H2) were utilized. The H2 probe was modified with Fc to allow for dual signal modulation. In the absence of the target, the hairpins remain in stable stem-loop conformations. Upon the introduction of miR-221, H1 is activated, thereby initiating a cascade reaction that continuously recycles the miRNA target while producing Fc-labeled H2. These Fc-tagged DNA strands are then captured by the electrode, leading to the simultaneous quenching of the ECL signal and the enhancement of the DPV signal due to redox activity.

In summary, BRAF V600E detection is based on ECL signal suppression via a TSDR-triggered "on-off" switch, while miR-221 detection relies on CHA-driven amplification to enable dual-mode signal output

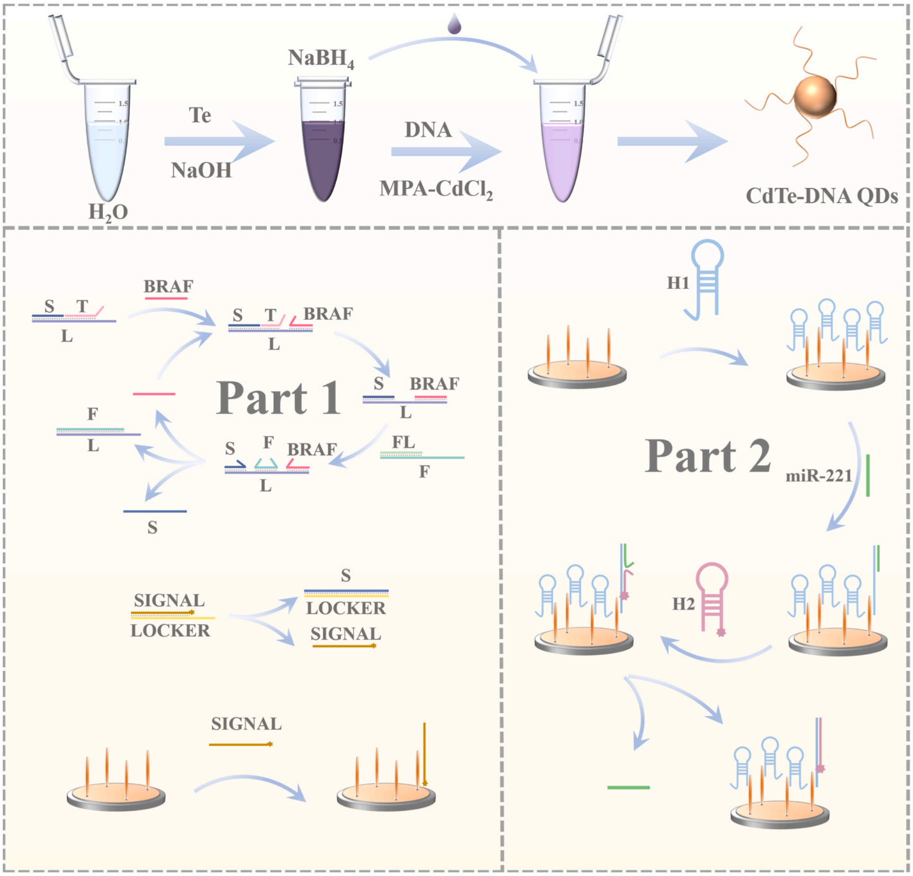

Scheme 1. Schematic illustration of the proposed dual-mode ECL biosensor. (A) Synthesis of CdTe-DNA QDs. (B) TSDR-based detection of BRAF V600E and release of Cy5-labeled signal strands. (C) CHA-based detection of miR-221 and Fc-mediated signal amplification.

(ECL quenching and DPV enhancement). This integrated sensing strategy can be utilized in the accurate diagnosis and subtype classification of PTC.

3.2. Characterization of CdTe-DNA QDs

The morphology of the CdTe-DNA QDs was characterized using

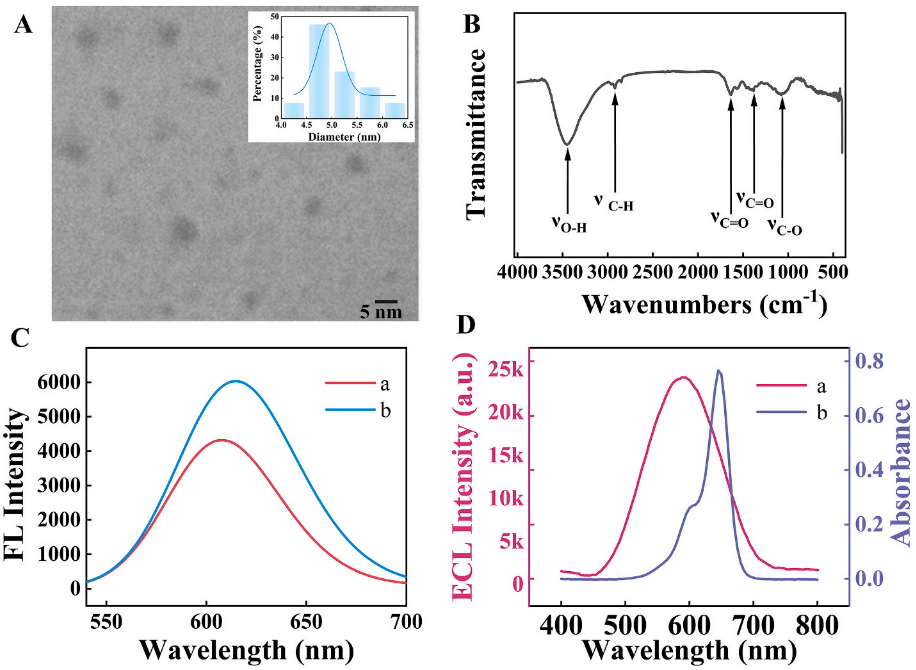

Fig. 1. Characterization of CdTe-DNA QDs. (A) TEM image of CdTe-DNA QDs. (B) FT-IR spectra of CdTe-DNA QDs. (C) Fluorescence spectra of CdTe QDs (curve a) and CdTe-DNA QDs (curve b). (D) ECL emission spectrum of CdTe-DNA QDs (curve a) and UV–vis absorption spectrum of Cy5 (curve b).

transmission electron microscopy (TEM). As shown in Fig. 1A, the QDs exhibited a spherical shape with an average diameter of approximately 5 nm and were uniformly dispersed throughout the field of view. The surface chemistry of the CdTe-DNA QDs was examined by Fourier-transform infrared (FT-IR) spectroscopy (Fig. 1B). The absorption band at 3457 cm^{-1} corresponds to the O–H stretching vibration, while that at 2919 cm^{-1} is attributed to the asymmetric stretching of C–H bonds. The peaks at 1629 cm^{-1} and 1384 cm^{-1} correspond to the asymmetric and symmetric stretching vibrations of C=O, respectively. The strong absorption peak at 1063 cm^{-1} is due to the symmetric stretching of C–O bonds, confirming the presence of carboxyl groups on the QD surface. Notably, the absence of absorption in the 2500–2650 cm^{-1} region indicates the disappearance of the S–H stretching vibration band, suggesting that the surface was successfully modified with MPA, in which an abundance of carboxyl groups were introduced (Tang et al., 2023). Fluorescence spectroscopy revealed the emission peak of unmodified CdTe QDs at 606 nm, and this peak was red-shifted to 615 nm in CdTe-DNA QDs (Fig. 1C) and was broader with enhanced intensity. This red shift and broadening of this peak are attributed to electrostatic interactions between the negatively charged DNA and positively charged QD surface, which reduce the interparticle distance and strengthen dipole–dipole interactions, leading to an increase in the Stokes shift. Furthermore, chemical bonding between thiolated DNA and surface Cd^{2+} disrupts the original surface passivation, generating additional non-radiative recombination centers that contribute to the observed broadening. However, DNA modification also passivates surface defects, leading to an overall increase in fluorescence intensity (Wei et al., 2015). To verify the occurrence of ECL resonance energy transfer (ECL-RET) between CdTe-DNA QDs and Cy5-labeled DNA, the emission spectrum of the CdTe-DNA QDs and the UV–vis absorption spectrum of Cy5 were analyzed (Fig. 1D). The maximum emission peak of the QDs was observed at 590 nm, while that of Cy5 spanned from 540 to 690 nm. This significant spectral overlap confirms the potential for efficient ECL-RET in this system.

3.3. Validation of sensor feasibility through ECL and DPV responses

The feasibility of the proposed biosensor was systematically evaluated using both ECL and DPV measurements. For BRAF V600E detection, ECL responses from variously modified electrodes were compared (Fig. 2A). The bare GCE exhibited negligible ECL signals (curve a), and modification with CdTe-DNA QDs significantly enhanced the signal (curve b). Further functionalization with Cy5-labeled probes could maintain strong ECL emission (curve c), representing the “signal-on” state. Upon the introduction of BRAF V600E, the TSDR mechanism was triggered, resulting in the release of Cy5-labeled signal strands, which were then captured by the electrode-immobilized probes. This interaction initiated ECL-RET between the CdTe QDs and Cy5, resulting in substantial quenching of the ECL signal (curve d), indicative of the “signal-off” state. This transition confirms the successful detection of the BRAF V600E mutation. For miR-221 detection, similar ECL analyses were performed (Fig. 2B). The bare GCE (curve a) showed minimal ECL signal, while the sequential assembly of CdTe-DNA QDs (curve b), H1 hairpins (curve c), and H2 hairpins (curve d) led to progressively enhanced signals in the absence of target, indicative of the “signal-on” state of the system. Upon the addition of miR-221, the CHA amplification reaction was activated, leading to the release of Fc-labeled H2 strands that were then captured by the electrode. This resulted in pronounced ECL quenching (curve e), demonstrating a clear target-responsive behavior. DPV measurements further validated the capability of the probe in miR-221 detection (Fig. 2C). In the absence of the target, the Fc oxidation current was negligible (curves a–d). Upon the addition of miR-221, the specific hybridization and capture of Fc-labeled strands generated a distinct DPV peak (curve e), confirming successful redox signal generation. These results collectively demonstrate that the biosensor had robust signal responsiveness and can exhibit dual-modality output during the detection of BRAF and miR-221.

3.4. Performance of the proposed biosensor in BRAF V600E detection

Under the optimal conditions, the ability of the biosensor to quantitatively detect BRAF V600E using an “on-off” ECL switching mechanism was evaluated. As shown in Fig. 3A, the ECL intensity progressively decreased with increasing BRAF V600E concentrations from 1 aM to 100 nM. Signal stability was confirmed by conducting three consecutive ECL scans at each concentration, and consistent signal profiles were obtained (Fig. 3B). A linear relationship between ECL intensity (I_{ECL}) and the logarithmic BRAF V600E concentration (lg c) was observed over the range of 10 aM to 1 nM (Fig. 3C). The regression equation was $I_{ECL} = -811.04 \lg c - 2818.35$, with a correlation coefficient (R^2) of 0.9953. The limit of detection (LOD), calculated using the 3σ criterion, was 5.21 aM. This low LOD indicates that the sensor has exceptional sensitivity and is suitable for trace-level detection. To assess specificity, control experiments were conducted using potential interfering species, including miR-155, miR-21, and miR-221 at 1 nM each (Fig. 3D). These non-target species led to negligible ECL quenching compared to the blank control, whereas 100 pM BRAF V600E resulted in a significant decrease in ECL signal. Moreover, when 100 pM BRAF V600E was mixed with excess concentrations (1 nM) of interfering RNAs, the ECL signal remained comparable to that of BRAF V600E alone, which confirms that the biosensor has high selectivity toward BRAF V600E. These results demonstrate that the proposed biosensor is ultra-sensitive and specific,

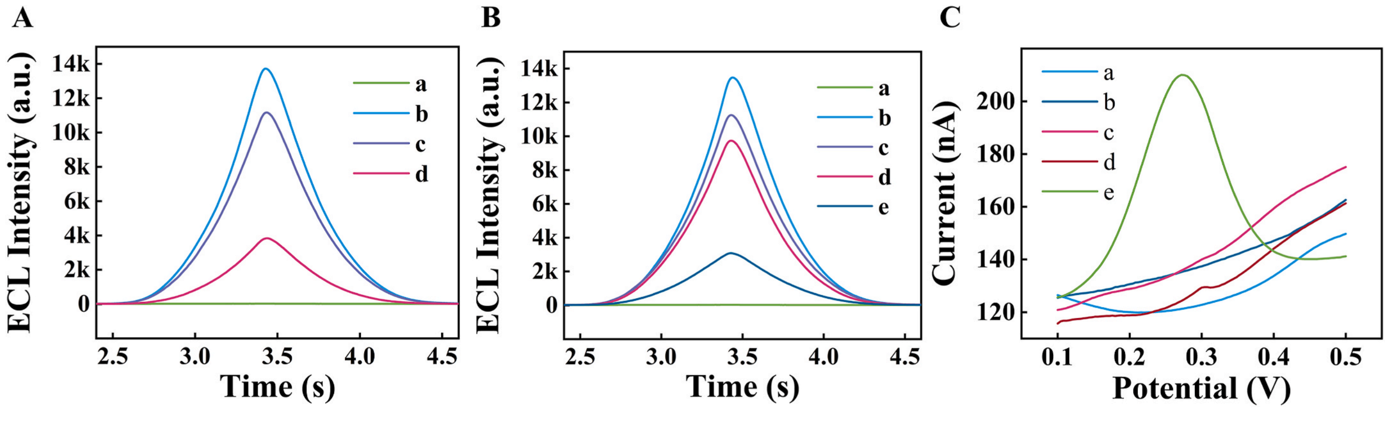

Fig. 2. Changes in ECL and DPV signals during sensor assembly and target detection. (A) ECL intensity-time curves for BRAF detection: (a) bare GCE, (b) GCE/CdTe-DNA QDs, (c) GCE/CdTe-DNA QDs/Cy5, (d) GCE/CdTe-DNA QDs/BRAF/Cy5. (B) ECL signal responses during miR-221 detection: (a) bare GCE, (b) GCE/CdTe-DNA QDs, (c) QDs + H1, (d) QDs + H1/H2, (e) QDs + H1/miR-221/H2. (C) DPV signals observed during miR-221 detection using the electrodes in (B).

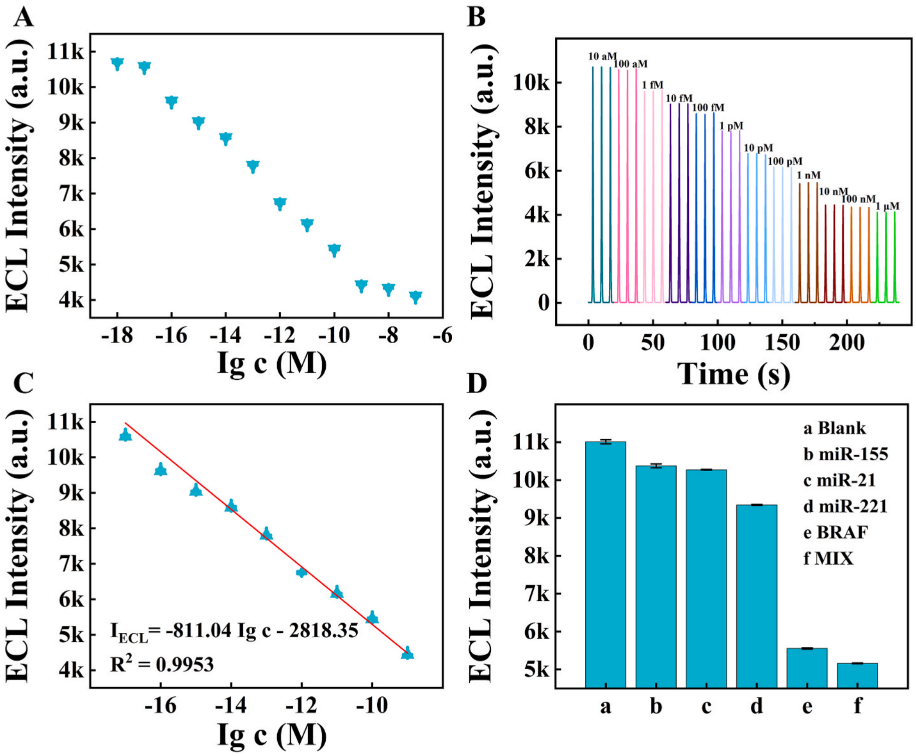

Fig. 3. Analytical performance of the biosensor in BRAF V600E detection. (A) ECL responses at different concentrations of BRAF V600E (1 aM-100 nM) with error bars representing standard deviations (n = 3, RSD <1 %). (B) Stability of ECL signals across three cycles. (C) Calibration curve showing the linear relationship between ECL intensity and lg[BRAF V600E] (n = 3, RSD <1 %). (D) Specificity analysis with miR-155, miR-21, and miR-221 (1 nM each) as potential interferents (n = 3, RSD <1 %).

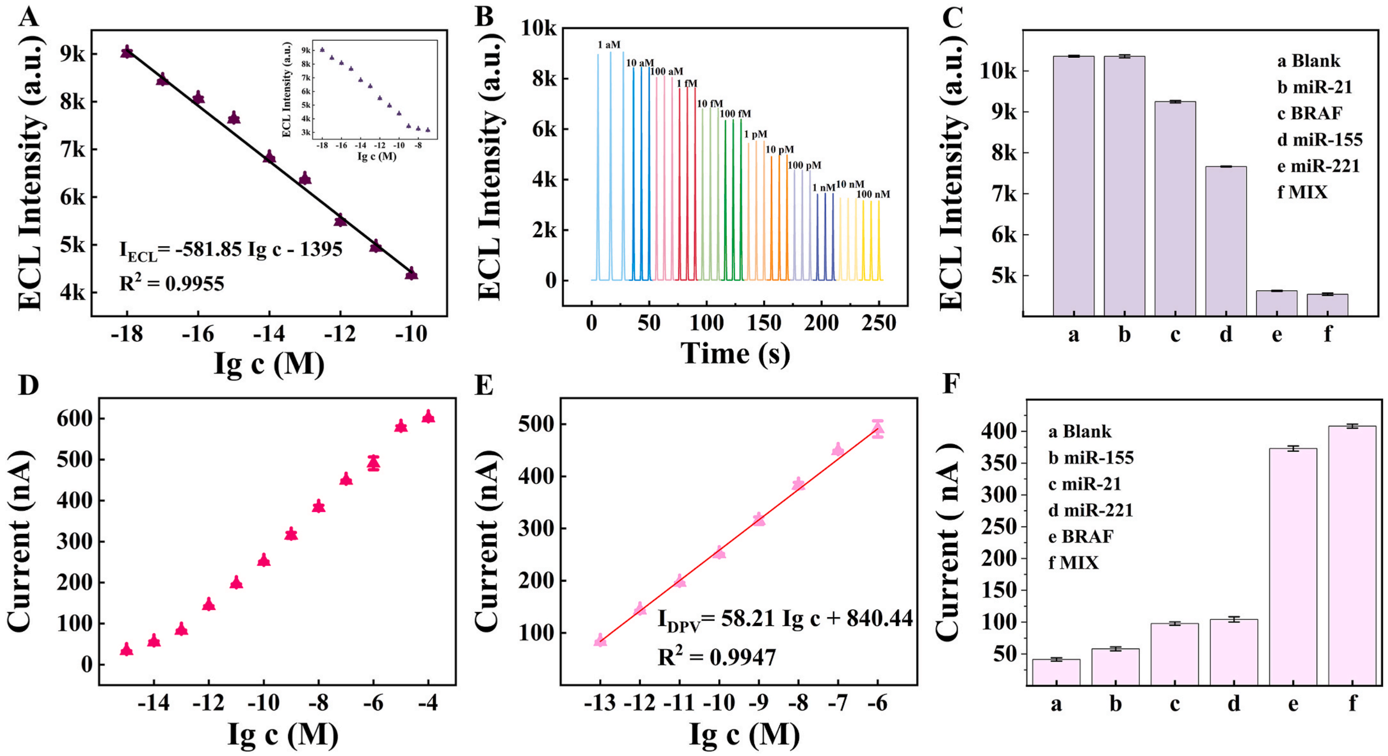

Fig. 4. Analytical performance of the biosensor in miR-221 detection. (A) ECL signal response at various concentrations of miR-221 (1 aM-100 nM) with error bars representing standard deviations (n = 3, RSD <1 %). (B) Stability of ECL signals across three cycles. (C) Specificity analysis by ECL with miR-155, miR-21, and BRAF V600E as interferents (n = 3, RSD <1 %). (D) DPV responses of miR-221 at different concentrations (1 fM-100 μM) with error bars (n = 3, RSD <6 %). (E) Calibration curve showing the linear relationship between DPV current and lg[miR-221] (n = 3, RSD <6 %). (F) Specificity analysis by DPV in the presence of interferents in (C) (n = 3, RSD <7 %).

has high performance in the detection of BRAF V600E, and can be a reliable molecular tool for thyroid cancer diagnostics. A comparison of the biosensor prepared in this experiment with other published literature (Table S3) showed that the biosensor had a lower detection limit and better sensitivity.

3.5. *Performance of the proposed biosensor in miR-221 detection*

The analytical performance of the biosensor in miR-221 detection was evaluated using both ECL and DPV methods. As shown in Fig. 4A, the ECL intensity decreased progressively with increasing miR-221 concentrations from 1 aM to 100 nM. The system generated stable and reproducible signals across all concentrations (Fig. 4B). A linear relationship was established between ECL intensity and the logarithm of miR-221 concentration over the range of 1 aM–100 pM, which yielded the regression equation $I_{ECL} = -581.85$ lg c -1395, with $R^2 = 0.9955$. The LOD, calculated using the 3σ method, was as low as 0.13 aM. DPV measurements were also performed to verify dual-signal output capability. As shown in Fig. 4D, the peak current of Fc increased proportionally with miR-221 concentrations ranging from 1 fM to 100 μM. A strong linear correlation between current intensity and lg c was observed over the concentration range of 100 fM to 1 μM (Fig. 4E), with the regression equation $I_{DPV} = 58.21$ lg c $+ 840.44$ and an R^2 of 0.9947. The LOD for DPV detection was calculated to be 23.0 fM. The specificity of the biosensor toward miR-221 was assessed using potential interfering species, including miR-155, miR-21, and BRAF V600E (1 nM each). As shown in Fig. 4C and F, the ECL and DPV signals of these groups were nearly identical to those of the blank control, while the signals generated in the presence of 100 pM miR-221 were distinctly different. Furthermore, in the presence of mixtures containing 10 nM miR-221 and 100 nM of interfering species, the sensor could maintain its signal integrity, which is indicative of excellent target selectivity and anti-interference capability. Collectively, these results highlight the ultra-high sensitivity, broad dynamic range, and robust specificity of the biosensor in miR-221 detection, validating its potential as a powerful tool for early molecular diagnosis of papillary thyroid carcinoma.

3.6. *Application in real samples*

To evaluate its clinical applicability, the proposed biosensor was employed to assess endogenous BRAF V600E and miR-221 levels in lysates of normal human thyroid cells (NHT) and thyroid cancer cells (TPC-1). For BRAF V600E detection, the ECL signal decreased with increasing number of TPC-1 cells in a concentration-dependent manner, and the signal induced by the lysate of NHT cells was significantly stronger than that caused by TPC-1(Fig. 5A). A similar trend was also observed in miR-221 detection. Although the ECL signal intensity of both cell lines decreased, the decrease in the TPC-1 lysate was more significant, and the intensity of the NHT samples was comparatively stronger (Fig. 5B). Further validation experiments were conducted using DPV analysis to quantify miR-221 levels. As shown in Fig. 5C, increasing concentrations of TPC-1 lysate progressively enhanced the intensity of the Fc oxidation peaks. By contrast, the DPV response of NHT lysates remained low and stable. This shows a clear distinction between cancerous and normal samples. The high consistency between ECL and DPV outputs confirms the robustness and reliability of the biosensor in detecting real biological samples. To further demonstrate clinical utility, standard addition recovery experiments were performed using human serum samples spiked with known concentrations of BRAF V600E or miR-221. For BRAF V600E, serum samples spiked with 100 aM, 10 fM, and 100 fM yielded recovery rates ranging from 98.68 % to 102.50 %. These high recovery rates indicate that the biosensor has high detection accuracy (Table S2). For miR-221, spiking experiments over three orders of magnitude (100 aM–100 fM) resulted in recovery rates of 94.60 %–107.05 % in ECL mode and 94.25 %–107.21 % in DPV mode (Table S2), validating the reliable performance of the biosensor in complex biological matrices. Collectively, these results demonstrate that the proposed biosensing platform an detect real biological samples, highlighting its translational potential for clinical diagnosis of thyroid cancer.

4. Conclusion

In summary, we developed a multifunctional ECL biosensor based on CdTe-DNA QDs for the sensitive detection and classification of PTC. The system has integrated capacities: enzyme-free DNA amplification and dual-mode signal transduction. The biosensor demonstrated excellent sensitivity, ultra-low detection limits (as low as the aM level), and high specificity. Moreover, its ability to reliably detect targets in complex biological samples (cell lysates and human serum) underscores its potential for real-world clinical diagnostics. The research successfully achieved the precise typing of PTC, the most common and most prevalent type of thyroid cancer, but the identification of other subtypes still requires further exploration. Future research will focus on establishing a more comprehensive classification system to achieve precise differential diagnosis of all subtypes of thyroid cancer.

CRediT authorship contribution statement

Yan Zhang: Writing – original draft, Investigation, Formal analysis, Data curation, Conceptualization. **Zhuoxin Ye:** Investigation, Data curation. **Mo Ma:** Investigation, Data curation. **Yongli Wu:**

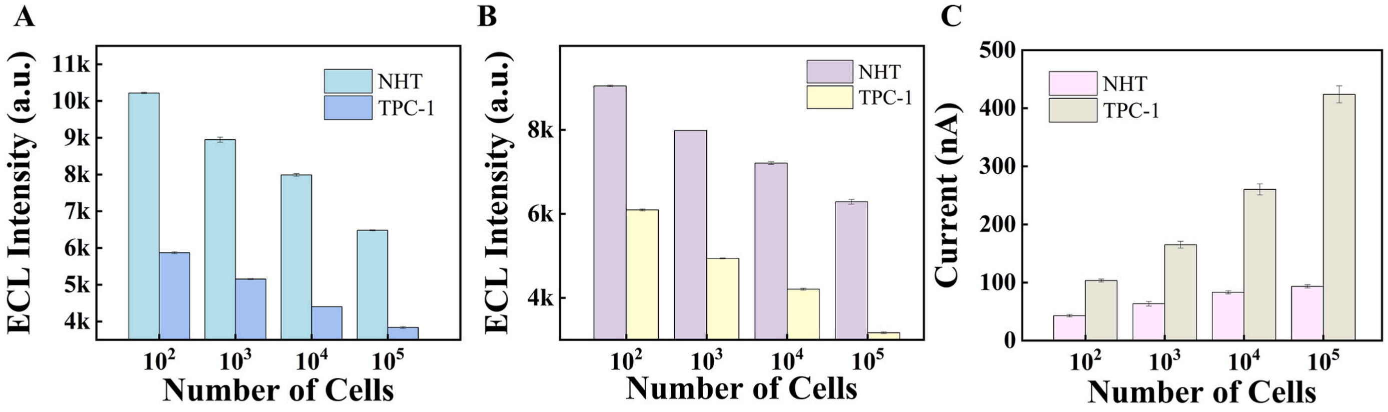

Fig. 5. Detection of BRAF V600E and miR-221 in real samples. (A) ECL signal responses for BRAF V600E in NHT and TPC-1 cell lysates (n = 3, RSD <1 %). (B) ECL signal responses for miR-221 in NHT and TPC-1 cell lysates (n = 3, RSD <1 %). (C) DPV current responses for miR-221 in NHT and TPC-1 cell lysates (n = 3, RSD <7 %).

Investigation, Data curation. **Yuxuan Chen:** Investigation, Data curation. **Ruiyan Liu:** Investigation, Data curation. **Pinyi Ma:** Writing – review & editing, Project administration, Data curation, Conceptualization. **Daqian Song:** Supervision, Resources, Funding acquisition, Conceptualization.

Declaration of competing interest

The authors declare that they have no known competing financial interests or personal relationships that could have appeared to influence the work reported in this paper.

Acknowledgments

This work was supported by the National Natural Science Foundation of China (22074052 and 22004046) and the Science and Technology Developing Foundation of Jilin Province of China (20240404044ZP).

Appendix A. Supplementary data

Supplementary data to this article can be found online at https://doi.org/10.1016/j.bios.2025.117964.

Data availability

Data will be made available on request.

References

Bikas, A., Vachhani, S., Jensen, K., Vasko, V., Burman, K.D., 2016. Targeted therapies in thyroid cancer: an extensive review of the literature. Expet Rev. Clin. Pharmacol. 9 (10), 1299–1313.

Boucai, L., Zafereo, M., Cabanillas, M.E., 2024. A review of thyroid cancer-reply. JAMA, J. Am. Med. Assoc. 331 (21), 1863–1864.

Brauckhoff, K., Biermann, M., 2020. Multimodal imaging of thyroid cancer. Curr. Opin. Endocrinol. Diabetes Obes. 27 (5), 335–344.

Bray, F., Laversanne, M., Sung, H.Y.A., Ferlay, J., Siegel, R.L., Soerjomataram, I., Jemal, A., 2024. Global cancer statistics 2022: GLOBOCAN estimates of incidence and mortality worldwide for 36 cancers in 185 countries. Ca-Cancer J. Clin. 74 (3), 229–263.

Cabanillas, M.E., McFadden, D.G., Durante, C., 2016. Thyroid cancer. Lancet 388 (10061), 2783–2795.

Cappola, A.R., 2017. How to look for thyroid cancer. JAMA, J. Am. Med. Assoc. 317 (18), 1840–1841.

Chen, Y.X., Ye, Z.X., Ma, M., Yang, J.K., Liu, R.Y., Zhang, Y., Ma, P.Y., Song, D.Q., 2024. Electrochemiluminescence biosensor for specific detection of pancreatic ductal carcinoma through dual targeting of MUC1 and miRNA-196a. Biosens. Bioelectron. 254, 116241.

Davis, S., Ullmann, T.M., Roman, S., 2023. Disparities in treatment for differentiated thyroid cancer. Thyroid 33 (3), 287–293.

Eilers, S.G., LaPolice, P., Mukunyadzi, P., Kapur, U., Wendel Spiczka, A., Shah, A., Saleh, H., Adeniran, A., Nunez, A., Balachandran, I., Clark, J.J., Lemon, L., 2014. Thyroid fine-needle aspiration cytology: performance data of neoplastic and malignant cases as identified from 1558 responses in the ASCP Non-GYN Assessment program thyroid fine-needle performance data. Cancer Cytopathology 122 (10), 745–750.

Giovanella, L., Deandreis, D., Vrachimis, A., Campenni, A., Ovcaricek, P.P., 2022. Molecular imaging and theragnostics of thyroid cancers. Cancers 14 (5), 1272–1294.

Haddad, R.I., Nasr, C., Bischoff, L., Busaidy, N.L., Byrd, D., Callender, G., Dickson, P., Duh, Q.Y., Ehya, H., Goldner, W., Haymart, M., Hoh, C., Hunt, J.P., Iagaru, A., Kandeel, F., Kopp, P., Lamonica, D.M., McIver, B., Raeburn, C.D., Ridge, J.A., Ringel, M.D., Scheri, R.P., Shah, J.P., Sippel, R., Smallridge, R.C., Sturgeon, C., Wang, T.N., Wirth, L.J., Wong, R.J., Johnson-Chilla, A., Hoffmann, K.G., Gurski, L. A., 2018. NCCN guidelines® insights Thyroid Carcinoma, version 2.2018 featured updates to the NCCN guidelines. J. Natl. Compr. Cancer Netw. 16 (12), 1429–1440.

Haugen, B.R., Alexander, E.K., Bible, K.C., Doherty, G.M., Mandel, S.J., Nikiforov, Y.E., Pacini, F., Randolph, G.W., Sawka, A.M., Schlumberger, M., Schuff, K.G., Sherman, S.I., Sosa, J.A., Steward, D.L., Tuttle, R.M., Wartofsky, L., 2016. 2015 American thyroid association management guidelines for adult patients with thyroid nodules and differentiated thyroid cancer the American thyroid association Guidelines task force on thyroid nodules and differentiated thyroid cancer. Thyroid 26 (1), 1–133.

Kouba, E., Ford, A., Brown, C.G., Yeh, C., Siegal, G.P., Manne, U., Eltoum, I.E., 2018. Detection of V600E mutations with next-generation sequencing in infarcted thyroid carcinomas after fine-needle aspiration. Am. J. Clin. Pathol. 150 (2), 177–185.

Kurt, B., Yalçin, S., Alagöz, E., Karslioglu, Y., Yigit, N., Günal, A., Deveci, M.S., 2012. The relationship of the BRAF mutation and the established prognostic factors in Papillary Thyroid carcinomas. Endocr. Pathol. 23 (3), 135–140.

Laukienė, R., Ambrozaityte, L., Cimbalistienė, L., Utkus, A., Tamosiunas, A.E., 2022. Diagnostic significance of FNAB miRNA expression in Papillary thyroid carcinoma. Diagnostics 12 (6), 1384–1398.

Lei, Y.-M., Wu, D., Pan, M.-C., Tao, X.-L., Zeng, W.-J., Gan, L.-Y., Chai, Y.-Q., Yuan, R., Zhuo, Y., 2024. Dynamic surface reconstruction of individual gold nanoclusters by using a co-reactant enables color-tunable electrochemiluminescence. Chem. Sci. 15 (9), 3255–3261.

Li, W., Liu, W., Yang, X., Liang, W.-B., Yuan, R., Zhuo, Y., 2024. Universal signal switch based on a Mesostructured Silica Xerogel-Confined ECL polymer for epigenetic quantification. Anal. Chem. 96 (4), 1651–1658.

Liang, L., Zheng, X.C., Hu, M.J., Cui, Y.J., Zhong, Q., Wang, S.Y., Huang, F., 2018. MiRNA-221/222 in thyroid cancer: a meta-analysis. Clin. Chim. Acta 484, 284–292.

Liu, D., Zhang, X., Zhao, J., Chen, S., Yuan, R., 2020. An ultrasensitive sensing platform for microRNA-155 based on H_2O_2 quenched hydroxide-dependent ECL emission of PFO Pdots. Biosens. Bioelectron. 150, 111872.

Maeda, T., Kato, H., Ando, T., Kawaguchi, M., Shibata, H., Ogawa, T., Noda, Y., Hyodo, F., Matsuo, M., 2025. MRI features of histological subtypes of thyroid cancer in comparison with CT findings: differentiation between anaplastic, poorly differentiated, and papillary thyroid carcinoma. Jpn. J. Radiol. 43 (2), 210–218.

Mahmoudian-Sani, M.R., Mehri-Ghahfarrokhi, A., Asadi-Samani, M., Mobini, G.R., 2017. Serum miRNAs as biomarkers for the diagnosis and prognosis of thyroid cancer: a comprehensive review of the literature. Eur. Thyroid J. 6 (4), 171–177.

McFadden, D.G., Vernon, A., Santiago, P.M., Martinez-McFaline, R., Bhutkar, A., Crowley, D.M., McMahon, M., Sadow, P.M., Jacks, T., 2014. p53 constrains progression to anaplastic thyroid carcinoma in a -mutant mouse model of papillary thyroid cancer. P Natl Acad Sci USA 111 (16), E1600–E1609.

Meng, X., Pang, X., Yang, J., Zhang, X., Dong, H., 2023. Recent advances in electrochemiluminescence biosensors for MicroRNA detection. Small 20 (22), 2307701.

Mishra, P.S., Yadav, D., Sharma, P.K., Malviya, R., 2023. Strategies for treatment of thyroid cancer. Curr. Drug Targets 24 (5), 406–415.

Park, J.-L., Kim, S.-K., Jeon, S., Jung, C.-K., Kim, Y.-S., 2021. MicroRNA profile for diagnostic and prognostic biomarkers in thyroid cancer. Cancers, 13040632.

Pellegrini, C., Di Nardo, L., Cipolloni, G., Martorelli, C., De Padova, M., Antonini, A., Maturo, M.G., Del Regno, L., Strafella, S., Micantonio, T., Leocata, P., Peris, K., Fargnoli, M.C., 2018. Heterogeneity of and promoter mutational status in Multiple Melanomas and Association with genotype. J. Mol. Diagn. 20 (1), 110–122.

Tan, J., Liu, R.Y., Zhu, G.W., Umbricht, C.B., Xing, M.Z., 2020. TERT promoter mutation determines apoptotic and therapeutic responses of BRAF-mutant cancers to BRAF and MEK inhibitors: Achilles Heel. P Natl Acad Sci USA 117 (27), 15846–15851.

Tang, Y., Liu, Y.W., Xia, Y.D., Zhao, F.Q., Zeng, B.Z., 2023. Simultaneous detection of ovarian cancer-concerned HE4 and CA125 markers based on Cu single-atom-triggered CdS QDs and Eu MOF@Isoluminol ECL. Anal. Chem. 95 (10), 4795–4802.

Tickoo, S.K., Pittas, A.G., Adler, M., Fazzari, M., Larson, S.M., Robbins, R.J., Rosai, J., 2000. Bone metastases from thyroid carcinoma - a histopathologic study with clinical correlates. Arch. Pathol. Lab Med. 124 (10), 1440–1447.

Tikhomirov, G., Hoogland, S., Lee, P.E., Fischer, A., Sargent, E.H., Kelley, S.O., 2011. DNA-based programming of quantum dot valency, self-assembly and luminescence. Nat. Nanotechnol. 6 (8), 485–490.

Veschi, V., Turdo, A., Modica, C., Verona, F., Di Franco, S., Gaggianesi, M., Tirrò, E., Di Bella, S., Iacono, M.L., Pantina, V.D., Porcelli, G., Mangiapane, L.R., Bianca, P., Rizzo, A., Sciacca, E., Pillitteri, I., Vella, V., Belfiore, A., Bongiorno, M.R., Pistone, G., Memeo, L., Colarossi, L., Giuffrida, D., Colarossi, C., Vigneri, P., Todaro, M., Stassi, G., 2023. Recapitulating thyroid cancer histotypes through engineering embryonic stem cells. Nat. Commun. 14 (1), 1351–1368.

Wang, Z.H., Yu, R.Z., Zeng, H., Wang, X.X., Luo, S.Z., Li, W.H., Luo, X.L., Yang, T., 2019. Nucleic acid-based ratiometric electrochemiluminescent, electrochemical and photoelectrochemical biosensors: a review. Microchim. Acta 186 (7), 405–424.

Wei, H.T., Fang, Y.J., Yuan, Y.B., Shen, L., Huang, J.S., 2015. Trap engineering of CdTe nanoparticle for high gain, fast response, and low noise P3HT:CdTe nanocomposite photodetectors. Adv. Mater. 27 (34), 4975–4981.

Wei, Y.X., Qi, H.L., Zhang, C.X., 2023. Recent advances and challenges in developing electrochemiluminescence biosensors for health analysis. Chem. Commun. 59 (24), 3507–3522.

Xu, L., Ma, M., Li, J., Dai, D., Gao, D., Ma, P., Wu, Q., Song, D., 2024. Exploration of aminopeptidase N as new biomarker for early diagnosis of thyroid cancer. Biosens. Bioelectron. 244, 115808.

Yang, L., Gu, X., Liu, J., Wu, L., Qin, Y., 2024. Functionalized nanomaterials-based electrochemiluminescent biosensors and their application in cancer biomarkers detection. Talanta 267, 125237.

Ye, Z.X., Liu, Y.B., Pan, M.C., Tao, X.L., Chen, Y.X., Ma, P.Y., Zhuo, Y., Song, D.Q., 2023. AgInZnS quantum dots as anodic emitters with strong and stable electrochemiluminescence for biosensing application. Biosens. Bioelectron. 228, 115219.

Yeh, M.W., Demircan, O., Ituarte, P., Clark, O.H., 2004. False-negative fine-needle aspiration cytology results delay treatment and adversely affect outcome in patients with thyroid carcinoma. Thyroid 14 (3), 207–215.

Zhang, S.Q., Ma, M., Zhao, C., Li, J.K., Xu, L.L., Zhang, Z.H., Diao, Q.P., Ma, P.Y., Song, D.Q., 2024. A novel low-background nitroreductase fluorescent probe for real-time fluorescence imaging and surgical guidance of thyroid cancer resection. Biosens. Bioelectron. 261, 116514.

Zhang, W., Xiong, H., Chen, M., Zhang, X., Wang, S., 2017. Surface-enhanced molecularly imprinted electrochemiluminescence sensor based on Ru@SiO$_2$ for ultrasensitive detection of fumonisin B1. Biosens. Bioelectron. 96, 55–61.

Zhou, J.J., Lv, X.Q., Jia, J.L., Din, Z.U., Cai, S.Q., He, J.L., Xie, F., Cai, J., 2022. Nanomaterials-Based electrochemiluminescence biosensors for food analysis: recent developments and future directions. Biosensors (Basel) 12 (11), 1046–1054.

Zhou, X., Zhang, W., Wang, Z., Han, J., Xie, G., Chen, S., 2020. Ultrasensitive aptasensing of insulin based on hollow porous $C_3N_4/S_2O_8^{2-}$/AuPtAg ECL ternary system and DNA walker amplification. Biosens. Bioelectron. 148, 111795.